

**Low temperature hydrothermal synthesis of Ni<sub>75</sub>Fe<sub>25</sub> nanostructured powders:  
microstructure, morphology and magnetic behaviour**

**A. Bouremana<sup>a</sup>, A. Guittoum<sup>b,\*</sup>, M. Hemmous<sup>b</sup>, D. Martínez-Blanco<sup>c</sup>,  
P. Gorria<sup>d</sup>, J. A. Blanco<sup>e</sup>**

a) Laboratory of Materials Physics, Faculty of Sciences, University of Science and Technology Houari Boumedienne (USTHB), Post-Box 32, El-Alia, Bab Ezzouar, Algiers, Algeria

b) Nuclear Research Centre of Algiers, 02 Boulevard Frantz Fanon, Post-Box 399, Alger-Gare, Algiers, Algeria

c) SCTs, University of Oviedo, EPM, 33600 Mieres (Spain)

d) Department of Physics & IUTA, EPI, University of Oviedo 33203 Gijón (Spain)

e) Department of Physics, University of Oviedo, Calvo Sotelo St., 33007 Oviedo (Spain)

**Abstract**

We have successfully synthesised Ni<sub>75</sub>Fe<sub>25</sub> nanostructured powders by means of low temperature (150 °C) hydrothermal method using sodium hydroxide (NaOH) as co-reduction agent. The powders are in fact large agglomerations of small nanoparticles with average diameters below 30 nm. The concentration of NaOH seems to play an important role in the final microstructure and morphology of the samples as deduced from scanning electron microscopy images. Although x-ray diffraction patterns reveal that the samples are single-phase with a face centered cubic crystal structure, the analysis of Mössbauer spectra suggests the existence of different local environments for the iron atoms. The room temperature saturation magnetization shows similar values for all the samples ( $\approx 90$  Am<sup>2</sup>/kg), in contrast with the coercive field that is clearly influenced by the morphology of the samples, ranging from 60 Oe (spherical-shaped samples) to 150 Oe (dendritic-shaped powders).

**Keywords:** Ni<sub>75</sub>Fe<sub>25</sub>; nanostructured powders; structure; microstructure; magnetic properties.

\*) aguittoum@gmail.com

## 1. Introduction

In the last two decades, magnetic nanomaterials have regained a huge interest due to the broad range of technological applications in which these materials are currently being used, such as micro-electronic devices, medical diagnosis, magnetic separation or catalysis among others [1-3]. Therefore, the optimization of the magnetic properties of metallic and metal-oxide nanoparticles (NPs) for any specific application requires a meticulous design and control of their composition and morphology (size, shape, state of aggregation, ...) [4-11]. In particular, Ni-rich NiFe binary alloys (commonly known as “Permalloys”) show an outstanding soft magnetic response for their use in high-density information storage, catalysis, chemical sensors or spintronic-based devices. [12-14]. However, the size reduction of the particles down to the nanometer length-scale together with the improvement of the magnetic response is often a challenging purpose.

Until now, several methods have been used to produce NiFe NPs with diverse morphologies and size distributions [15-20]. The hydrothermal method is particularly interesting because of its low cost, surfactant-free procedure and simplicity, but also because there are multiple parameters that can be optimized during the synthesis process in order to modify the shape and size of the nanoparticles and consequently their magnetic properties [21-24]. Nevertheless, the hydrothermal route (i.e, the co-reduction of nickel and iron salts) to obtain binary NiFe alloys is not free from complications because the transformation of the iron salts into stable hydroxides that are difficult to reduce must be avoided. Moreover, the difference between the reduction potential of nickel and iron may lead to the occurrence of phase segregation. Therefore, the synthesis of NiFe nanoparticles with enhanced magnetic behaviour still remains as a stimulating and incompletely resolved issue; hence, the key parameters involved in such chemical processes need further optimization. Among these parameters, the use of sodium hydroxide, NaOH, seems to be essential to co-reduce the metallic salts and facilitate the formation of the alloy thus circumventing the segregation of spurious phases [25,26]. In this work, we focus our efforts mainly on the effect that the amount of NaOH have on the formation of Ni<sub>75</sub>Fe<sub>25</sub> nanoparticles by hydrothermal process. We will show how the microstructure and morphology of

Ni<sub>75</sub>Fe<sub>25</sub> nanoparticles governs the hyperfine field distributions as well as the magnetic properties of the system.

## 2. Experimental

For the synthesis of Ni<sub>75</sub>Fe<sub>25</sub> NPs a solution of 22.5 mL is first prepared by dissolving 0.71 g of NiCl<sub>2</sub>•6H<sub>2</sub>O and 0.27g FeCl<sub>3</sub>•6H<sub>2</sub>O in ethanol/water mixing solution (V/V: 3/1) and a molar ratio of nickel to iron of 3:1 (chemicals supplied from Sigma Aldrich). Afterwards, 7.5 mL of N<sub>2</sub>H<sub>4</sub>•H<sub>2</sub>O (hydrate hydrazine 86 %) containing 1g of NaOH is added drop wise to the above solution under vigorous stirring for 20 min. The mixed solution was loaded into a sealed Teflon cup, maintained at 150 °C for 2h and then cooled down to room temperature. The black fluffy product at bottom of the solution was collected using a magnetic bar, and cleaned with distilled water and absolute ethanol. The process was repeated several times in order to remove any reminiscent alkali salt and/or impurities. The final product was dried in air at 40 °C for 4 h. A series of four powder samples was prepared with different amount of NaOH (1, 2, 4 and 5 g), and will be named as S-1, S-2, S-4 and S-5, respectively.

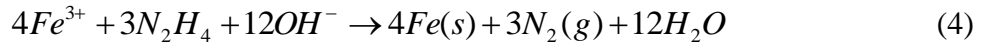
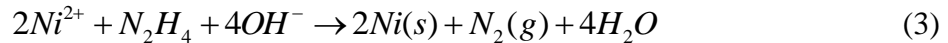
The morphology of the samples was visualized through several micrographs obtained with a JEOL JSM-6610LV scanning electron microscope (SEM) equipped with Energy Dispersive X-ray (EDX) analyser. The X-ray diffraction (XRD) patterns were collected by means of a PANalytical X-Pert Pro PW3050/60 diffractometer using a Cu anode ( $\lambda = 1.5406\text{\AA}$ ) over an angular range from 30° to 110° in  $2\theta$  with a step of 0.05°. The full profile analysis of the diffraction patterns was performed using the MAUD software based on the Rietveld method combined with a Fourier analysis [27, 29], with rather good reliability factors. We have used the Popa model incorporated in MAUD software [30, 31] in order to estimate the average crystallite size from the width of the Bragg diffraction peaks. Room temperature Mössbauer spectra in transmission mode were collected with a Wissel spectrometer using a <sup>57</sup>Co(Rh) source. A metallic iron foil was used for energy calibration and also as a reference for the isomer shift. Mössbauer spectra were analysed with the Recoil software using the Voigt-based hyperfine field distribution method (HFD-VB-F) [32], and the fit of the spectra was

performed with the half-width at half-maximum (HWHM) of the lines as free parameters. Room temperature magnetization vs. applied magnetic field,  $M(H)$ , curves were measured in a MicroSense vibrating sample magnetometer (VSM, model EV9) in the  $\pm 22$  kOe range. Up to 450 data points were collected for each  $M(H)$  curve in order to determine with high accuracy the coercive field as well as the saturation magnetization of the samples.

### 3. Results and Discussion

#### 3.1. Mechanisms of NiFe formation and chemical composition

The synthesis of NiFe nanoparticles can be described as follow. First, the solid hydroxides  $M(OH)_2$  ( $M=Ni, Fe$ ) are formed when the hydrazine mixed with NaOH is added to the mixture solution of  $NiCl_2$  and  $FeCl_3$ . The chemical reactions can be written as [26]:



Therefore, we may conclude that during the growth process of NiFe particles the iron and nickel salts are reduced by hydrazine hydrate in a concentrated basic medium. The capability of  $Fe(OH)_3$  and  $Ni(OH)_2$  to release  $Fe^{3+}$  and  $Ni^{2+}$  diminishes if the concentration of NaOH is excessive, hence, the formation of  $Fe^{3+}$  and  $Ni^{2+}$  free ions in the solution is not favoured, giving rise to a lower Ni-Fe crystal growth rate and a concomitant difficulty for the formation of  $FeNi_3$  phase [33].

The chemical composition of the samples was deduced from EDX analysis. The obtained atomic percentage of Ni and Fe is about 74% and 26%, respectively, for all the samples, being in excellent agreement with the ratio of the starting solution (experimental error around 1%). In addition to nickel and iron peaks, some traces of oxygen and carbon are also observed.

### 3.2. Crystal structure, morphology and microstructural analysis

The images depicted in Figure 1 evidence that the morphology of the samples depends on the concentration of NaOH. For the lowest concentration, sample S-1, the images show quasi-spherical entities, with average diameters ranging from 0.5 to 1  $\mu\text{m}$ , that are composed of a large number of aggregated smaller particles with sizes well below 100 nm (see Figs. 1a and 1b). By increasing the NaOH concentration the morphology changes drastically to snow-like shaped entities (see Figures 2c and 2d for sample S-2) and no spherical objects are found. Indeed, each of these entities is composed of several main branches and every of them have smaller branches distributed on both sides. In sample S-4 the entities take the morphology of leaf-pine-like (see Figures 2e and 2f). However, if the concentration is increased to 5g (sample S-5), quasi-spherical-shaped entities appear again with similar sizes (between 0.5 and 1  $\mu\text{m}$ ) and morphology (each entity is composed of many smaller particles, see Figures 2g and 2h) to those observed in sample S-1. From the above observations, we can assume that the concentration of the alkali agent, NaOH, plays a major role in the final morphology of the  $\text{Ni}_{75}\text{Fe}_{25}$  samples.

The XRD patterns corresponding to the four  $\text{Ni}_{75}\text{Fe}_{25}$  samples are depicted in Figure 3 together with the Rietveld fit. The five observed diffraction peaks can be indexed as the (111), (200), (220), (311) and (222) Bragg reflections of a  $\text{Ni}_{75}\text{Fe}_{25}$  disordered solid solution with face centred cubic (fcc) crystal structure [34, 35]. The absence of any additional Bragg reflections rules out the existence of any ordered  $\text{Ni}_3\text{Fe}$  phase with simple cubic ( $Pm\bar{3}m$ ) crystal structure [36]. The values for the lattice parameter and the anisotropic crystallite size were estimated from the Rietveld refinement of the XRD patterns (see Table 1). It is worth noting that, the value of the lattice parameter,  $a \approx 3.552 \text{ \AA}$ , does not change with the concentration of NaOH, and coincides with the data for pure  $\text{Ni}_3\text{Fe}$  alloy according to the JCPDS card (N° 65-3244). The latter corroborates that the stoichiometry of the samples is  $\text{Ni}_{75}\text{Fe}_{25}$  as already obtained from EDX analysis.

The broad shape of the diffraction peaks is a clear signature of the nanostructured character of the samples. The value for the mean crystallite size,  $\langle D \rangle$ , has been estimated from the Rietveld

refinement of the XRD patterns. Assuming an anisotropic geometry of the crystallites we have obtained the value of the mean crystallite size for different crystallographic orientations (see table 1). In all the four samples the value corresponding to the (111) Bragg reflection,  $\langle D \rangle_{111}$  is the largest one and almost double than that obtained for the (200), (220) and (311) ones. It is worth noting that such differences are larger for samples S-2 and S-4 with dendritic (snow- or life-pine-like) shaped entities observed in SEM images (see Figure 2).cHowever, the change in the values for the mean crystallite sizes estimated from the different Bragg reflections is not so remarkable for the other two samples, S-1 and S-5, showing spherical shaped agglomerates (see Figures 2a, 2b, 2g and 2h), thus suggesting that the nanocrystals are more isotropic.

### 3.3. Mössbauer spectroscopy

In figure 4 the room temperature Mössbauer spectra for all the samples together with the hyperfine field distributions (HFD) obtained from the fits are depicted. A characteristic sextet typical of ferromagnetic materials is present in the four spectra. However, it is important to note the significant broadening of the spectral lines if compared with those of a bcc-Fe foil. This fact is commonly associated with differences in the local environment of the Fe atoms in  $\text{Ni}_3\text{Fe}$  due to a certain degree of disorder in the material that gives rise to a distribution of hyperfine fields [36-40].

The hyperfine field distribution obtained from the fit shows three different components for all the investigated samples. In a disordered  $\text{Ni}_{75}\text{Fe}_{25}$  solid solution each Fe atom has in average 3 Fe atoms as next neighbours (nn), however, the probability to find Fe atoms with either 2 or 4 Fe nn is far from being negligible. Therefore, we can assign the three observed components as coming from Fe atoms with 4 nn ( $H_{\text{hf}} \approx 300$  kOe); with 3 nn ( $H_{\text{hf}} \approx 276$  kOe) and with 2 nn ( $H_{\text{hf}} < 200$  kOe). In addition, a singlet with a minority contribution (below 7% in all the cases) is needed to properly fit the spectra, probably due to some Fe atoms with reduced number of Fe nn (less than 2) in paramagnetic state. The results obtained from the fit of the Mössbauer spectra are summarized in Table 2.

If we focus our attention on the right hand side of Figure 4 and on data in Table 2, we can realize that the hyperfine field distributions display the same main features for all the samples, although there are some slight variations concerning the height of the high- $H_{\text{hf}}$  shoulder, the width of the low- $H_{\text{hf}}$  peak and the mean values of  $H_{\text{hf}}$ . These changes in the hyperfine field distributions can be ascribed to different percentages of iron atoms with 2, 3 and 4 Fe next neighbours.

### 3.4. Magnetic properties

In Figure 5 we plot the magnetization curves,  $M(H)$ , of the four samples, the full hysteresis loops (upper panel) together with an enlarged view of the low magnetic field region (lower panel), that confirm the ferromagnetic character at room temperature. The magnitude of the saturation magnetization,  $M_s$ , has been estimated by fitting the high magnetic field region of the hysteresis loop to an approach-to-saturation behaviour [41]. The values of  $M_s$  as well as those for the coercive field,  $H_c$ , are gathered in table 3. The hysteresis loops look almost saturated for  $H > 10$  kOe, with  $M_s$  values around  $90 \text{ Am}^2/\text{kg}$  for all the samples, which are comparable to those found by other authors for NiFe NPs synthesized by hydrothermal method with different morphologies: spheres [42] ( $85.2 \text{ Am}^2/\text{kg}$  and  $66 \text{ Oe}$ ), snow-like [35] ( $89.6 \text{ Am}^2/\text{kg}$  and  $156 \text{ Oe}$ ), leaf-like [43] ( $93.2 \text{ Am}^2/\text{kg}$  and  $180.5 \text{ Oe}$ ).

However, the low field region of the hysteresis loops (see Figure 5b) shows that the coercive field is clearly smaller for the samples S-1 and S-5 with spherical shaped agglomerates ( $\approx 60 \text{ Oe}$ ), if compared with samples S-2 and S-3 with snow- or leaf-like dendritic morphologies ( $H_c > 120 \text{ Oe}$ ). These findings evidence a strong correlation between the low-field region of the  $M(H)$  curves and the morphology of the samples either at the micrometer as well as at the nanometer length-scales. We may continue to remember at this point that the mean size of the nanocrystals forming the agglomerates are far from being spherical for samples exhibiting dendritic powders, thus suggesting that the magnetic anisotropy is mainly governed by the sample microstructure and morphology.

## 4. Summary and conclusions

We have successfully synthesized pure Ni<sub>75</sub>Fe<sub>25</sub> powder following a low cost and surfactant-free hydrothermal method at relative low temperatures (150° C) and moderately short annealing periods (2 hours) by using sodium hydroxide (NaOH). The SEM images evidence different morphologies depending on the amount of NaOH, let's say, the micrometer sized powders take a spherical shape for the higher(5g) and the lower (1g) NaOH quantity, while dendritic morphologies are found for 2g and 4g, respectively. The analysis of the XRD patterns confirms that all the samples are Ni<sub>75</sub>Fe<sub>25</sub> disordered solid solutions with fcc crystal structure and a value of the lattice parameter slightly larger than 3.55 Å. Mössbauer spectroscopy reveals the existence of different local environments for the Fe atoms giving rise to a distribution of hyperfine fields with three major contributions, thus ruling out the formation of a Ni<sub>3</sub>Fe ordered phase. Moreover, the line-broadening analysis of the XRD patterns tells us that the nanocrystals forming the powders have an average size below 30 nm, although they are larger and with non-spherical shapes for the samples with snow- and leaf-pine-like powder morphology. The latter has not a clear influence on the value of the saturation magnetization (around 90 Am<sup>2</sup>/kg), but determines the magnitude of the magnetic shape anisotropy of the system and therefore, sets up directly the coercive field of the samples.

## 5. References

- [1] P. Moriarty, Rep. Prog. Phys. 64 (2001) 297.
- [2] D.L. Huber, Small. 1 (2005) 482.
- [3] Q. A. Pankhurst, J. Connolly, S.K. Jones, J. Dobson, J. Phys. D: Appl. Phys. 36 (2003) R167.
- [4] A. H. Haviv, J.M. Greneche, J.-P. Lellouche, J. Am. Chem. Soc. 132 (2010) 12519.
- [5] M.P. Fernandez-Garcia, P. Gorria, M. Sevilla, M.P. Proenca, R. Boada, J. Chaboy, A.B. Fuertes, J.A. Blanco, J. Phys. Chem. C, 115 (2011) 5294.
- [6] M. Estrader et al., Nature Commun., 4 (2013) 2960.
- [7] N. Rinaldi-Montes et al., Nanoscale, 6 (2014) 457.
- [8] A. Biffis, N. Orlandi, B. Corain, Adv. Mater. 15 (2003) 1551.



- [9] N. Rinaldi-Montes, P. Gorria, D. Martínez-Blanco, Z. Amghouz, A.B. Fuertes, L. Fernandez-Barquin, I. de Pedro, L. Olivi, J.A. Blanco, *J. Mater. Chem. C*, 3 (2015) 5674.
- [10] Y. Mao, J. Parsons, J.S. McCloy, *Nanoscale*, 5 (2013) 4720.
- [11] M.P. Fernández-García, P. Gorria, J.A. Blanco, A.B. Fuertes, M. Sevilla, R. Boada, J. Chaboy, D.S. Schmool, J.-M. Grenèche, *Phys. Rev. B*. 81 (2010) 094418.
- [12] J.T. Tian, C.H. Gong, L.G. Yu, Z.S. Wu, Z.J. Zhang, *Chin. Chem. Lett.* 19 (2008) 1123.
- [13] Y. I. Golovin, D.Y. Golovin, A.V. Shuklinov, R.A. Stolyarov, V.M. Vasyukov, *Tech. Phys. Lett.* 37 (2011) 253.
- [14] Y. Liu, Y. Chi, S. Shan, J. Yin, J. Luo, C.J. Zhong, *J. Alloy. Comp.* 587 (2014) 260.
- [15] Y.B. Feng, T. Qiu, *J. Alloys Comp.* 513 (2012) 455.
- [16] Z. Xu, C. Jin, A. Xia, J. Zhang, G. Zhu, *J. Magn. Magn. Mater.* 336 (2013) 14.
- [17] Y. Liu, Y. Chi, S. Shan, J. Yin, J. Luo, C.J. Zhong, *J. Alloys Comp.* 587 (2014) 260.
- [18] J.C. Jia, J. C. Yu, Y.X. J. Wang, K. M. Chan, *ACS Appl. Mater. Interfaces.* 2 (2010) 2579.
- [19] M. A. A. Mohamed, *Mat. Sci. Eng. B.* 190 (2014) 7.
- [20] J.M. Le Breton, O. Isnard, J. Juraszek, V. Pop, I. Chicinas, *Intermetallics.* 35 (2013) 128.
- [21] Q. Liao, R. Tannenbaum, Z.L. Wang, *J. Phys. Chem. B.* 110 (2006) 14262.
- [22] A. Bouremana, A. Guittoum, M. Hemmous, B. Rahal, J.J. Sunol, D. Martínez-Blanco, J.A. Blanco, P. Gorria, N. Benrekaa, *J. Magn. Magn. Mater.* 11 (2014) 358.
- [23] H. Chen, C. Xu, G. Zhao, Y. Liu, *Mat. Letters.* 91 (2013) 75.
- [24] A. Bouremana, A. Guittoum, M. Hemmous, D. Martínez-Blanco, J.A. Blanco, P. Gorria, N. Benrekaa, *Mater. Chem. Phys.* 160 (2015) 435.
- [25] X. Su, H.G. Zheng, Z.P. Yang, Y.C. Zhu, A.L. Pan, *J. Mater. Sci.* 38 (2003) 4581.
- [26] L.J. Liu, J.G. Guan, W.D. Shi, Z.G. Sun, J.S. Zhao, *J. Phys. Chem. C.* 114 (2010) 13565.
- [27] L. Lutterotti, S. Matthies, H.-R. Wenk, *IUCr: Newsletter of the CPD* 21 (1999) 14. (<http://www.ing.unitn.it/~maud/>).
- [28] H. M. Rietveld, *J. Appl. Cryst.* 22 (1969) 65.

- [29] R.A. Young, *The Rietveld Method*, Oxford University Press/IUCr, Oxford, 1993.
- [30] N.C. Popa, *J. Appl. Cryst.* 31 (1998) 176.
- [31] D. Martinez-Blanco, P. Gorria, J.A. Blanco, M.J. Perez, J. Campo, *J. Phys.: Condens. Matter.* 20 (2008) 335213.
- [32] K. Lagarek, D. Rancourt, Recoil Software, Physics Department, University of Ottawa, 1998.
- [33] X.M. Zhou, X.W. Wei, *Cryst. Growth. Design.* 9 (2009) 7.
- [34] A. Datta, M. Pal, D. Chakravorty, D. Das, S.N. Chintalapudi, *J. Magn. Magn. Mater.* 205 (1999) 301.
- [35] Y. Sun, Q. Liang, Y. Zhang, Y. Tian, Y. Liu, F. Li, D. Fang, *J. Magn. Magn. Mater.* 332 (2013) 85.
- [36] T.E. Cranshaw, *J. Phys. F: Met. Phys.* 17 (1987) 967.
- [37] J.W. Drijver, F.van der Woude, S. Radelaar, *Phys. Rev. B.* 16 (1977) 985.
- [38] J. Restrepo, G.A. Pérez Alcázar, A. Bohórquez, *J. Appl. Phys.* 81 (1997) 4101.
- [39] E. Jartych, *J. Magn. Magn. Mater.* 265 (2003) 176.
- [40] K. Brzózka, D. Olekšáková, P. Kollár, T. Szumiata, B. Górká, M. Gawroński, *Hyperf. Interact.* 168 (2006) 1091.
- [41] B.D. Cullity, *Introduction to Magnetic Materials*, Addison-Wesley, Reading MA, 2009.
- [42] S.J. Yan, L. Zhen, C.Y. Xu, J.T. Jiang, W.Z. Shao, *J. Phys. D: Appl. Phys.* 43 (2010) 245003.
- [43] Y. Cao, S.G. Ai, J. Zhang, N. Gu, S. Hu, *Adv. Mater. Lett.* 4 (2013) 160.

### Table captions

**Table 1.** Values of the lattice parameters,  $a(\text{Å})$ , and average crystallite size,  $\langle D \rangle_{\text{hkl}}(\text{nm})$ , of  $\text{Ni}_{75}\text{Fe}_{25}$  NPs samples obtained from the Rietveld refinement of the XRD patterns together with the reliability factors of the fit.

**Table 2.** Summary of the values obtained from the fit of the room temperature Mossbauer spectra of  $\text{Ni}_{75}\text{Fe}_{25}$  NPs samples.

**Table 3.** Estimated values of the saturation magnetization and coercive field for the five  $\text{Ni}_{75}\text{Fe}_{25}$  NPs samples.

### Figure captions

**Figure 1.** Example of EDX spectrum for the sample S-5 elaborated with 5g of NaOH.

**Figure 2.** SEM images of the  $\text{Ni}_{75}\text{Fe}_{25}$  NPs samples. Figures (a)-(b), (c)-(d), (e)-(f) and (g)-(h) correspond to samples S-1, S-2, S-4 and S-5, respectively.

**Figure 3.** Observed (dots) and calculated (solid line) room temperature XRD patterns of the  $\text{Ni}_{75}\text{Fe}_{25}$  samples. The small vertical bars indicate the location of the Bragg reflections. The observed-calculated difference appears at the bottom of each pattern.

**Figure 4.** Room temperature Mössbauer spectra for the  $\text{Ni}_{75}\text{Fe}_{25}$  samples and their corresponding hyperfine field distributions obtained from the fit of the spectra (see text for details).

**Figure 5.** (a) Room temperature hysteresis loops for the  $\text{Ni}_{75}\text{Fe}_{25}$  NPs samples. (b) Zoom of the low applied magnetic field region.

**Table 1**

<b>SAMPLE</b>	<b>a (Å)</b>	<b>&lt;D&gt;<sub>111</sub></b> <b>(nm)</b>	<b>&lt;D&gt;<sub>200</sub></b> <b>(nm)</b>	<b>&lt;D&gt;<sub>220</sub></b> <b>(nm)</b>	<b>&lt;D&gt;<sub>311</sub></b> <b>(nm)</b>	<b>&lt;D&gt;<sub>222</sub></b> <b>(nm)</b>	<b>R<sub>wp</sub>(%)</b>	<b>R<sub>exp</sub>(%)</b>
S-1	3.5527(2)	14(1)	8(1)	9(1)	8(1)	14(1)	9.9	6.9
S-2	3.5584(2)	24(1)	9(1)	12(1)	12(1)	24(1)	12.5	7.1
S-4	3.5530(2)	25(1)	11(1)	14(1)	13(1)	25(1)	9.8	6.9
S-5	3.5551(2)	19(1)	10(1)	12(1)	10(1)	19(1)	9.2	6.9

**Table 2**

<b>SAMPLE</b>	<b>Area (%)</b>	<b>Components</b>	<b>Relative intensity (%)</b>	<b>&lt;IS&gt; (mm/s)</b>	<b>&lt;QS&gt; (mm/s)</b>	<b>&lt;H<sub>hf</sub>&gt; (kOe)</b>	<b>&lt; H<sub>hf</sub>&gt; (kOe)</b>
S-1	94	1	30.5	0.02	0.00	27.6(1)	27.7(5)
		2	56			30.3(5)	
		3	13.5			17.0(4)	
S-2	94	1	50	0.02	0.00	27.9(4)	27.6(9)
		2	34			31.6(9)	
		3	16			18.2(9)	
S-4	96	1	20	0.02	0.00	27.6(1)	27.2(8)
		2	57			30.1(3)	
		3	23			19.5(9)	
S-5	97	1	21	0.02	0.00	27.6(1)	28.9(8)
		2	74			30.1(4)	
		3	5			17.0(1)	

**Table 3**

<b>SAMPLE</b>	<b>M<sub>s</sub> (emu/g)</b>	<b>H<sub>c</sub> (Oe)</b>
S-1	89(2)	60(3)
S-2	91(2)	149(3)
S-4	91(2)	126(3)
S-5	98(2)	60(3)

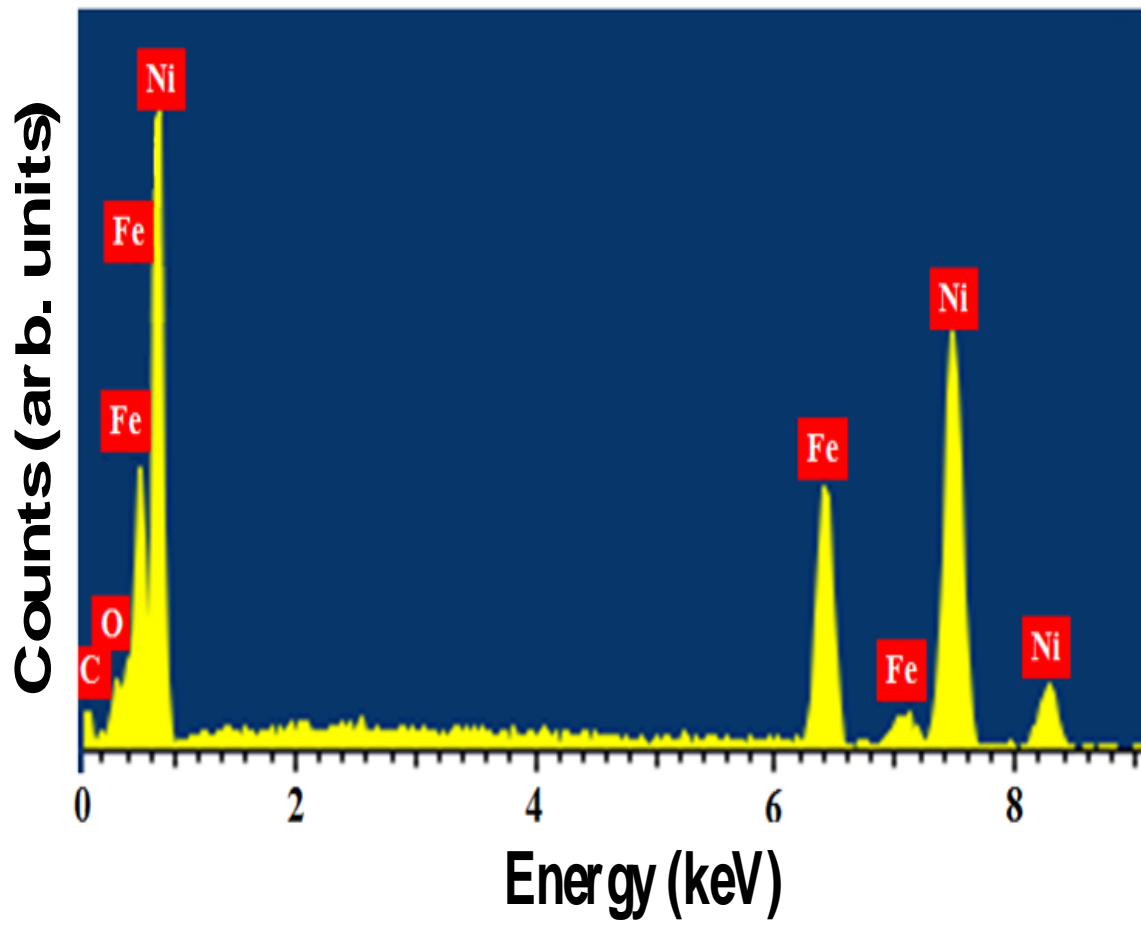
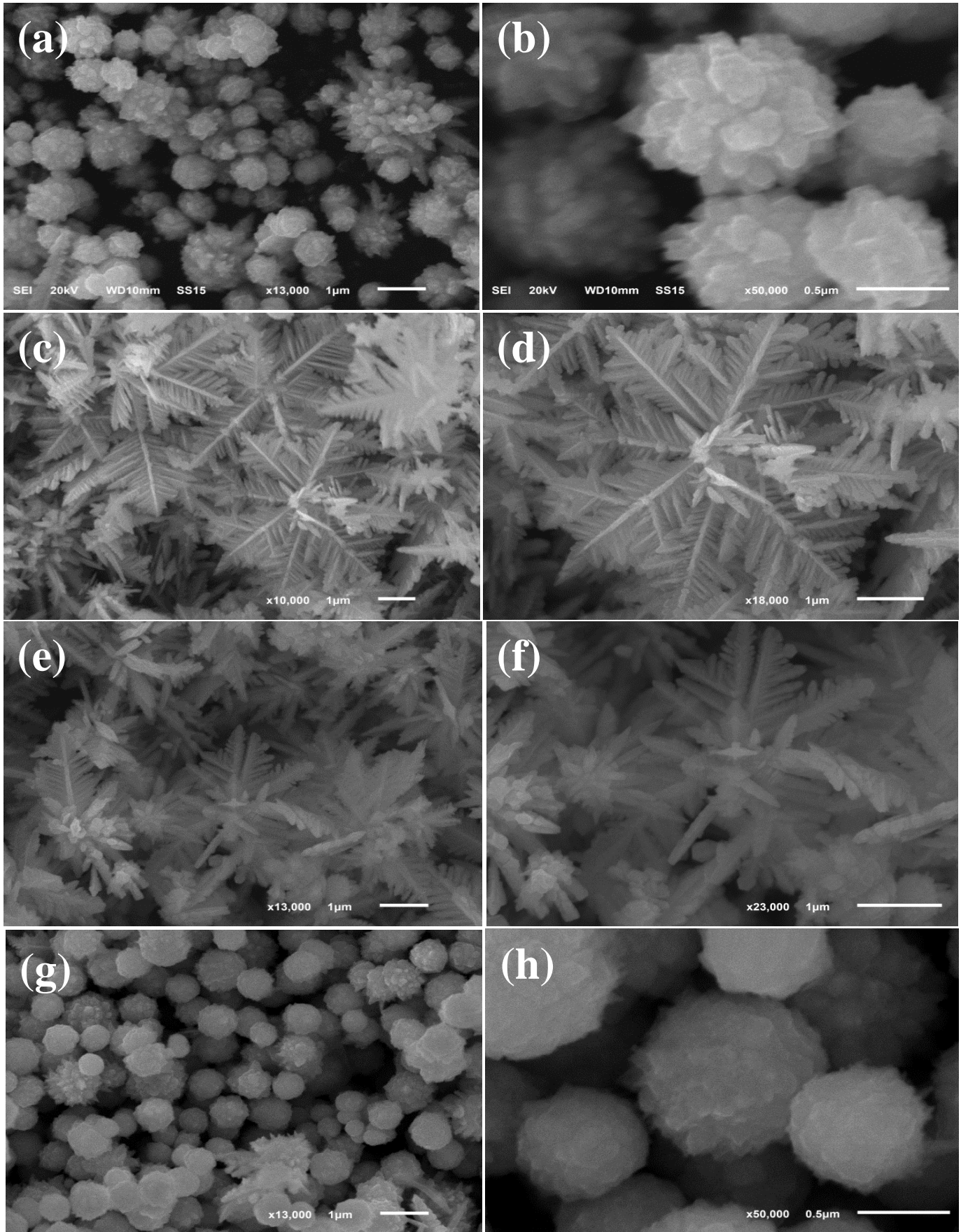


Figure 1



**Figure 2**

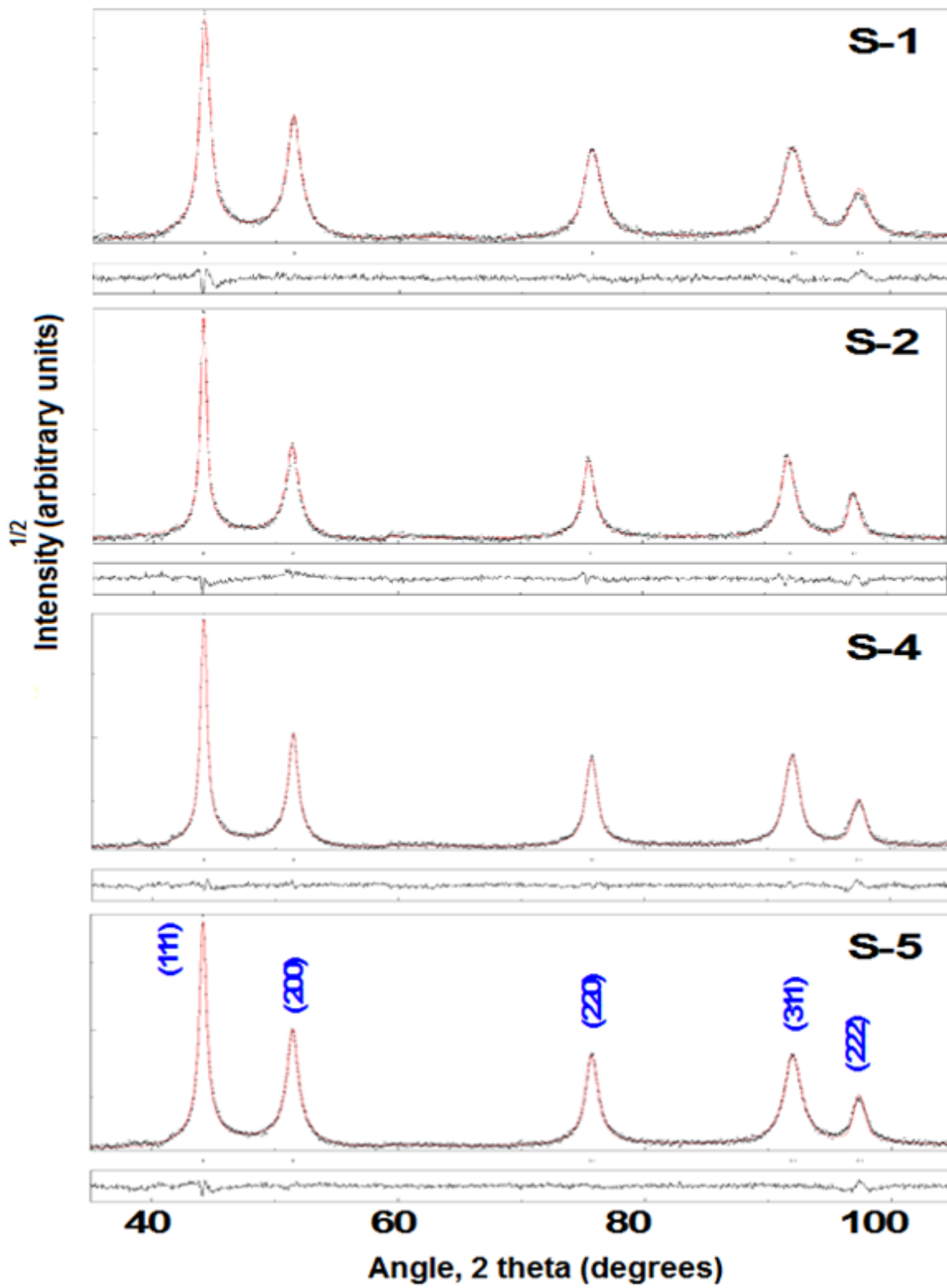


Figure 3

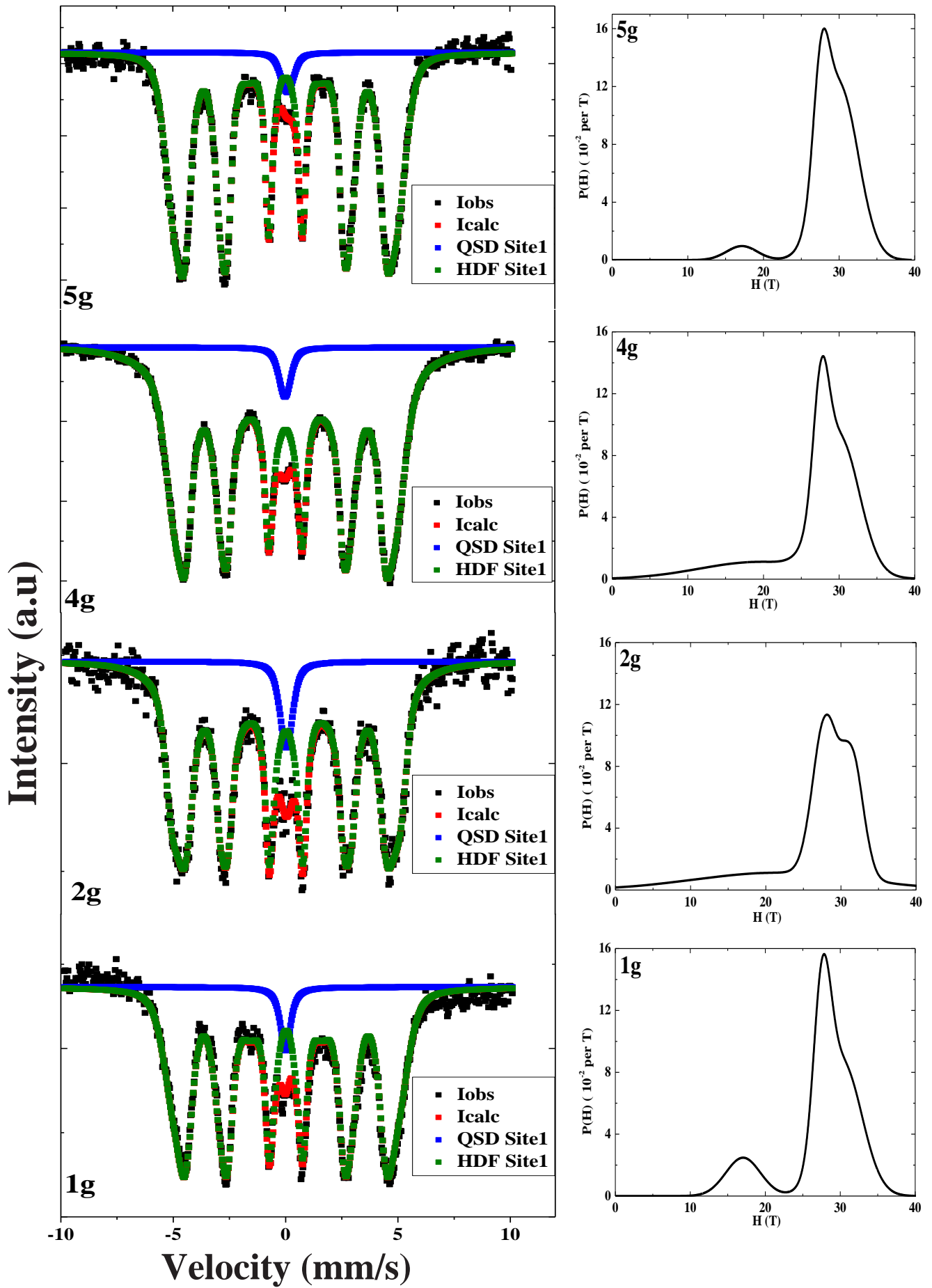


Figure 4



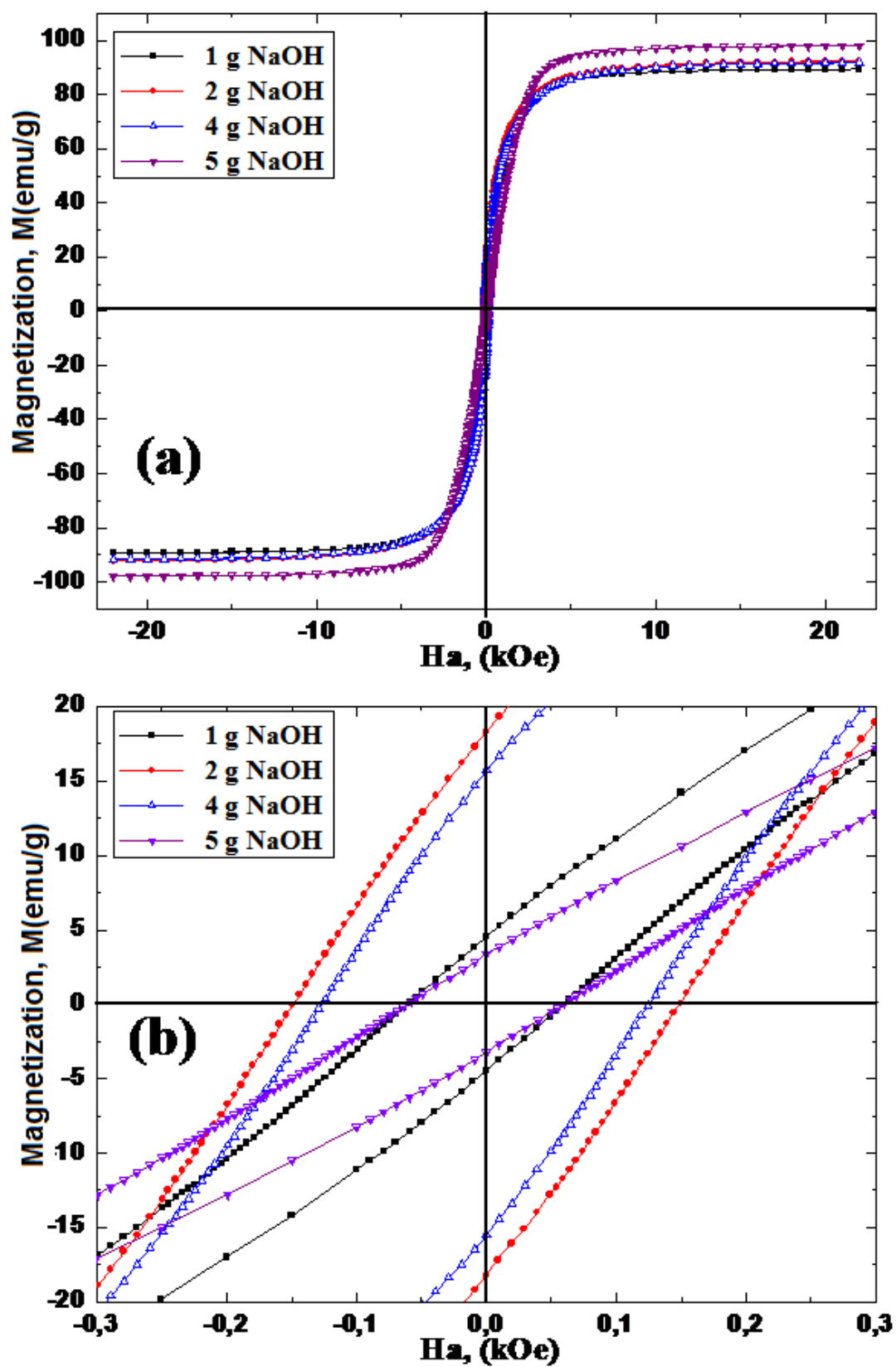


Figure 5